# Wall-Resolved Large-Eddy Simulation of Supercritical Airfoil Side-Edge Noise

Guang C. Deng[1,2,*], Satoshi Baba[1], Stéphane Moreau[2], Philippe Lavoie[1]

[1]Institute for Aerospace Studies, University of Toronto, Toronto, Canada
[2]Mechanical Engineering, Université de Sherbrooke, Sherbrooke, Canada
[*]patrickgc.deng@mail.utoronto.ca

*Abstract—*

A wall-resolved compressible large-eddy simulation and wind-tunnel experiments are performed on a finite-span supercitical airfoil to investigate the side-edge flow structures and noise sources. The geometry is composed of an isolated supercritical profile (2% camber, 13% thickness) with finite span. The chordwise Reynolds number is 620,000 and the free-stream Mach number is 0.09. The aerodynamic results obtained with a compressible unstructured Large Eddy Simulation solver show the development of turbulent structures from the boundary layer on the airfoil, along with the trajectory of the primary and secondary vorticies. Surface wall shear stress pathlines are compared with experimental oil-flow visualization results yielding good agreement, especially at flow impingement locations. Wall RMS pressure contours highlight the side-edge shear layer and flow impingement of the primary vortex at the pressure side edge to be important noise generation mechanisms. The Ffowcs Williams and Hawkings analogy is used to compute the far-field noise levels. The aeroacoustics simulation results are then compared to the experimental results.

*Keywords-component—***LES, CAA, Airfoil Noise**

## I. INTRODUCTION

Aircraft noise pollution is a growing concern in urban areas worldwide, due to its environmental impacts and potential health consequences. While aircraft engines were once the main source of noise, recent design improvements in turbofan engines have reduced their noise emissions, shifting the focus of research to airframe noise as the next dominant source [1]. Airframe noise is broadband in nature and generated primarily from the landing gear, slat, flap side-edges, and trailing edges [2]. The current study focuses on side-edge noise due to its high-intensity emissions. Mitigating aircraft noise – specifically airframe noise – is necessary to facilitate the transition to green and sustainable aviation industry.

Side-edge noise results from a complex combination of multiple flow structures in its vicinity, each responsible for broadband and/or tonal noise at different frequency ranges. Two of the notable flow structures are the side-edge shear layer and tip vortex impingement, which both originate from the pressure difference between the pressure and suction sides [2]–[4]. One of the key flow structures that contribute to side-edge noise is the Kelvin-Helmholtz instability, which occurs at the shear layer between the high-speed flow on the suction side of the airfoil and the slower flow on the pressure side. This instability leads to the formation of vortices that break down into smaller-scale turbulent structures. These smaller vortices create pressure fluctuations as they interact with the surrounding air, which then radiate noise. Another important flow structure is the tip vortex impingement, which is generated by the interaction of the tip vortex and the airfoil surface resulting in unsteady pressure fluctuations radiating sound waves [5], [6]. Although the flow structures at the side-edge are generally well defined, there still exists a lack of understanding about the underlying noise generation mechanism behind these main flow structures and dependencies on flow parameters such as angle of attack and Reynolds number.

The aim of the present study is to analyze the side-edge noise around a supercritical cantilever wing with compressible wall-resolved large-eddy simulation (LES) in order to investigate the tip-noise sources. First, an uRANS simulation of the full geometry is performed in order to visualize the time-averaged flow structures and to initialize the LES. Then the LES of a 40% reduced span with tip gap is performed. Finally, the Ffowcs Williams and Hawkings (FW-H) analogy

is applied to propagate the far-field acoustics. Comparisons with experiments of surface flow visualizations and far-field acoustics are presented.

## II. SETUP

The numerical domain is based on the experimental configuration at the University of Toronto Insitute for Aerospace Studies (UTIAS) Hybrid Aneochic Wind Tunnel (HAWT) with a single cantilever wing of supercritical profile (2% Camber, 13% thickness) [7]. The compressible solver AVBP v7.9 developed at CERFACS is used for the present LES [8]. The computational domain is $11.7\,c \times 2.72\,c \times 0.98\,c$ and is shown in Fig. 1. The angle of attack is set at $\alpha = 5°$ and the inlet velocity is set at $U_\infty = 30$ m/s corresponding to the chord based Reynolds number of $Re_c = 620,000$ and freestream Mach number of 0.09. To reduce the computational cost, the airfoil span and tip gap is reduced to 40% of the experimental setup. The midspan as well as the tip pressure and wake velocity, are compared with the previous uRANS results in Sec. III.
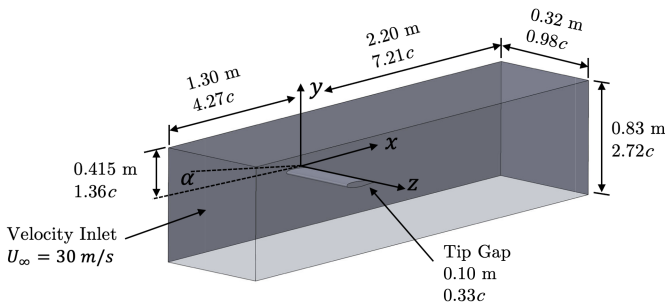
Figure. 1: Simulation domain and geometry for LES.

The numerical scheme applied in the present computation is the Lax-Wendroff scheme, which is second-order both in space and time [9]. The time step is fixed at $1.25 \times 10^{-8}$ s, providing a maximum Courant–Friedrichs–Lewy (CFL) number of 0.7. The wall-adapting local eddy-viscosity model (WALE) was used for a subgrid scale model to ensure proper turbulence decay towards the wall. The Navier–Stokes characteristic nonreflective boundary condition (NSCBC) are used at the inlet and the outlet [10], combined with sponge layers to avoid spurious reflections. The airfoil walls are modelled as no-slip adiabatic walls while the tunnel side walls are modelled as free-slip adiabatic walls.

The applied mesh shown in Fig. 2 is hybrid, unstructured and composed of $162 \times 10^6$ cells. It is specifically refined in the wake and at the side edge to capture the development of turbulent flow structures. The airfoil is meshed with 18 prismatic layers with a stretching ratio of 1.13 with 3950 nodes along the chord. The wall resolution in wall units is within the range of $x^+ < 40$, $z^+ < 40$, $y^+ < 3$ with 98% of cells below $y^+ = 1.5$, therefore meeting the criteria for a wall-resolved simulation [11].

An uRANS simulation was performed on the same mesh to initialize the LES with the solver ANSYS CFX V19.1 [12]. The $k - \omega$ shear stress transport model was used to
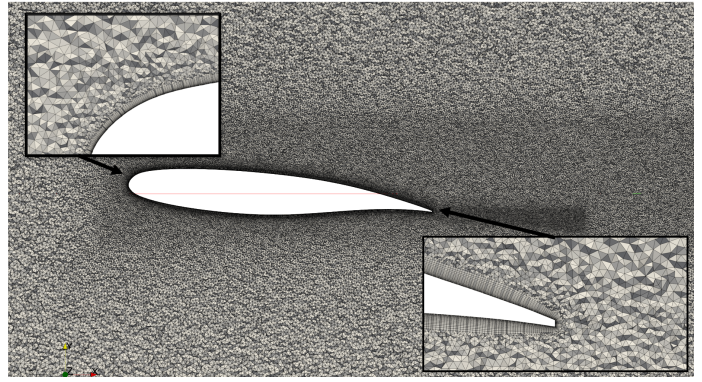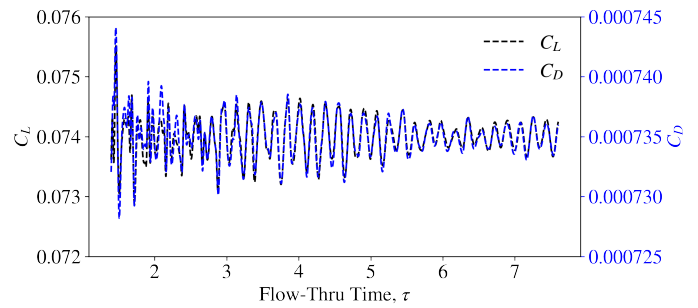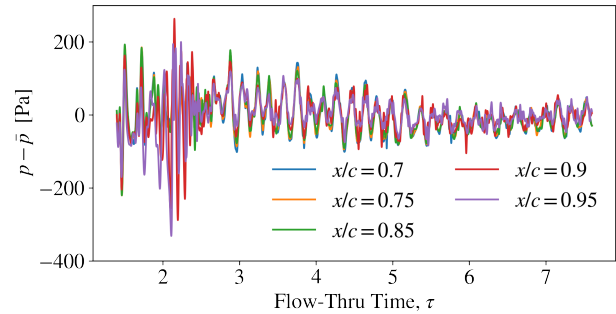
Figure. 2: Zoomed in views of the LES mesh at $0.02c$ from the side edge.

Figure. 3: Global and local time signals - a) airfoil lift and drag coefficient, b) fluctuating pressure of 5 probes on airfoil suction side midspan.

simulate the turbulence. Convection, transient, and turbulence model equations were resolved with second-order schemes. After establishing the flow for 6 chordwise flow-through times (84 ms), statistics for wall-pressure were extracted from the simulation during approximately 20 ms (two flowthrough times based on the chord) for the FW-H analogy. The end of the transient period is determined using a method based on local quantities from Mockett *et al.* [13] for statistical error estimation of finite time signals.

Global convergence has been monitored through the time evolution of the lift and drag coefficient shown in Fig. 3a, while the local convergence has been checked with various probes located on the airfoil surface, vortex core, and wake. An example of local convergence is shown in Fig. 3b illustrating

the local convergence of various probes along the airfoil midspan. The flow is stabilized after three flow through times, which corresponds to roughly 30 ms. The computation was performed using the supercomputer Niagara from Compute Canada, managed by SciNet. A total of 40 nodes, each with 40 Intel Skylake cores at 2.4 GHz, was used for computing 20 ms simulation time, for the total CPU time of 220 h.

## III. AERODYNAMICS RESULTS

### A. Flow Topology

Isosurfaces of the $Q$-criterion, the second invariant of the velocity gradient tensor, coloured by streamwise velocity are shown in Fig. 4a for the mean field and Fig. 4b for the instantaneous field. The primary vortex emanates from the pressure side shear layer and is initially located on the side edge, while the secondary vortex labelled in blue emanates from the suction side shear layer and is initially located on the suction surface. The pressure and suction side shear layers feed energy to the primary and secondary vortices and are formed due to boundary layer separation at both pressure and suction side corners. At $x/c = 0.5$, the primary vortex rolls up and detaches from the side edge, while the secondary vortex grows inboard in the spanwise direction. Near $x/c = 0.75$, the primary vortex begins crossing over to the suction surface to merge with the secondary vortex due to the pressure gradient at the side edge. During the vortex crossover, the primary vortex impinges on the suction surface and side edge, leaving a trail of low pressure peaks. Furthermore, a tertiary vortex traced in red forms near the trailing-edge pressure side after the primary vortex has detached from the side edge. After the tertiary vortex forms, it is quickly drawn to merge with the secondary vortex again due to the high pressure gradient at the side edge.

### B. Surface Pressure

The comparison between the uRANS and WR-LES cases is shown in Fig. 5 for the average streamwise pressure coefficient $Cp$ at three spanwise locations. The $C_p$ at $0.01c$ from the tip is altered by three low-pressure peaks on the suction side from $x/c = 0$ to $x/c = 0.8$, labelled A, B and C, respectively. A is the leading-edge suction peak. B is created by flow impingement from the secondary vortex. C is created by the primary vortex after crossing over to the suction side surface. The suction peaks B and C, induced by the impingement of the secondary and primary vortices on the suction surface, provide valuable information on the location and intensity of flow impingement at the side-edge, which is a potential source of unsteady pressure fluctuations and noise generation.

As noted in Sec. II, the LES was performed with a geometry with its span reduced to 40% of the experimental wind tunnel model to reduce the computational cost. As shown in Fig. 5, this span reduction in the LES case compared to the full-span configuration in the uRANS case is expected to have limited impact on the flow at the midspan and tip region. Overall, there is good agreement between the uRANS and WR-LES cases.
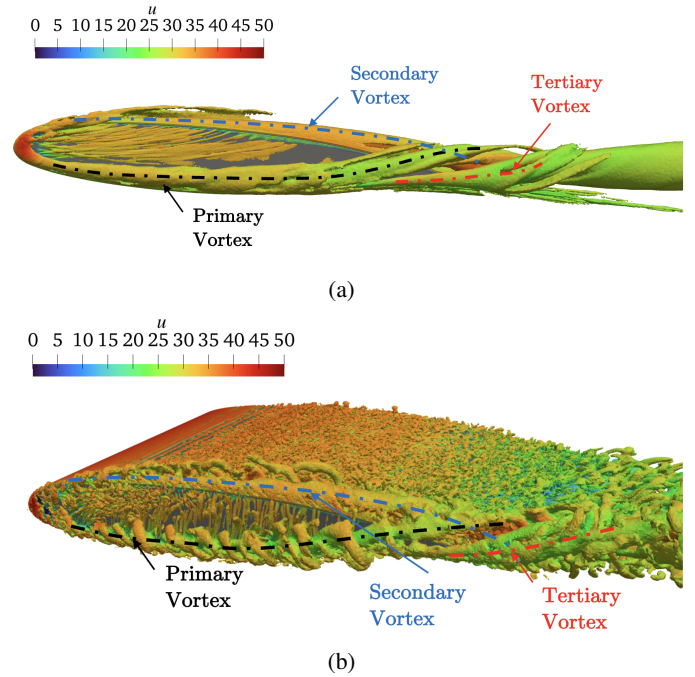


(a)



(b)

Figure. 4: Isocontour of the Q–Criterion ($2 \times 10^5 s^{-2}$), $\alpha = 5°$, $Re = 6.2 \times 10^5$, $Ma = 0.09$, color normalized by the mean streamwise velocity - a) mean isocontour averaged over 1 flow-through time, b) instantaneous isocontour.
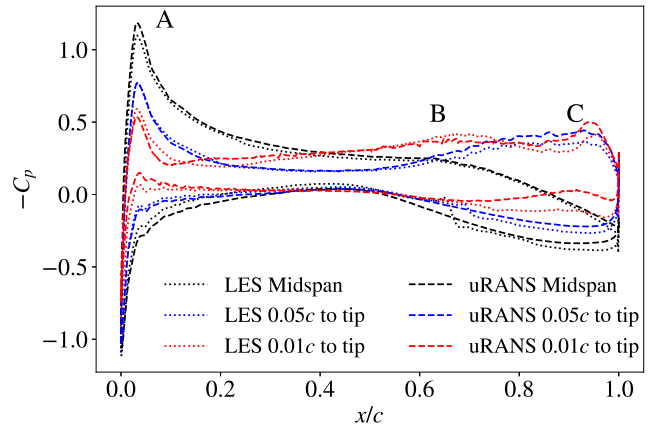


Figure. 5: Mean pressure coefficient comparison between uRANS results (dash) and LES results (solid).

The root mean square (RMS) wall pressure contour is shown in Fig. 6. At the side edge, the influence of the primary and secondary vorticies are clearly visible as regions of high RMS pressure that follow the trajectory of the primary flow separation line shown in Fig. 7. The region of high RMS pressure on the suction surface also agrees with suction peaks B and C in the $C_p$ curve. The maximum RMS pressure occurs near the leading edge where the incoming flow attaches to the side edge, perpetuating the development of pressure and suction side shear layers. This highlights the potential of the side-edge shear layer as a significant noise source. Additionally,

a significant RMS pressure area can be seen at the blunt trailing edge tip, where the tertiary vortex interacts with the blunt trailing edge. As a result, the vortex inertia is modified and scattered by the trailing edge, causing unsteady pressure fluctuations in this region. This interaction between the tip-vortex system and the trailing edge represent a potentially significant noise generation mechanism in addition to shear-layer development and flow impingement.
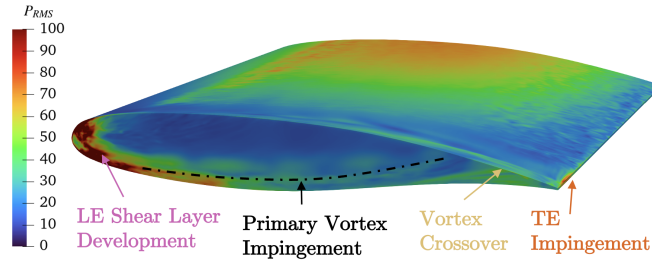


Figure. 6: RMS Pressure on the airfoil surface.

## C. Surface flow Visualization

Figure 7 presents surface flow visualization results from both LES simulations and experimental oil flow visualization, demonstrating good agreement in the tip and suction surface flow profiles and separation lines. The surface flow patterns provide insight regarding regions of vortex flow impingement which is a main acoustic generation mechanism. The flow separates from the leading edge and impinges on the focal point at $0.065c$, convecting towards the suction surface as it travels down the chord. Although no significant vortex structures are observed, small separation lines are seen on the suction and pressure sides near the leading edge. The suction side near the trailing edge shows a separation line, indicating that the vortex on the tip surface is convected to the side edge. Furthermore, the flow profile indicates that the chordwise flow is convected inboard due to the pressure difference between the tip surface and the suction surface, driving the generation of the side-edge vortex system. Overall, there is good agreement in the flow separation line profiles from both computational and experimental results.

## IV. AEROACOUSTIC RESULTS

### A. Nearfield Dilatation

The dilatation field, defined as $(-1/\rho \times \partial\rho/\partial t)$, was extracted from the simulation to obtain the nearfield wave patterns generated by the airfoil. The dilatation field at $0.06c$ from the tip shown in Fig. 8a depicts three main acoustic sources. First, a dominant source is seen at the trailing edge due to the scattering of boundary layer turbulence. Second, a source is seen at the leading edge due to flow impingement. Third, the side-edge vortex can also be seen propagating weaker wave fronts upstream. Wave interference from the three acoustic sources can be seen on the suction side. The dilatation field at $0.95c$ from the trailing edge shown in Fig. 8b displays the wave front generated by the tip vortex in the streamwise direction. While the dilatation field is mostly dominated by
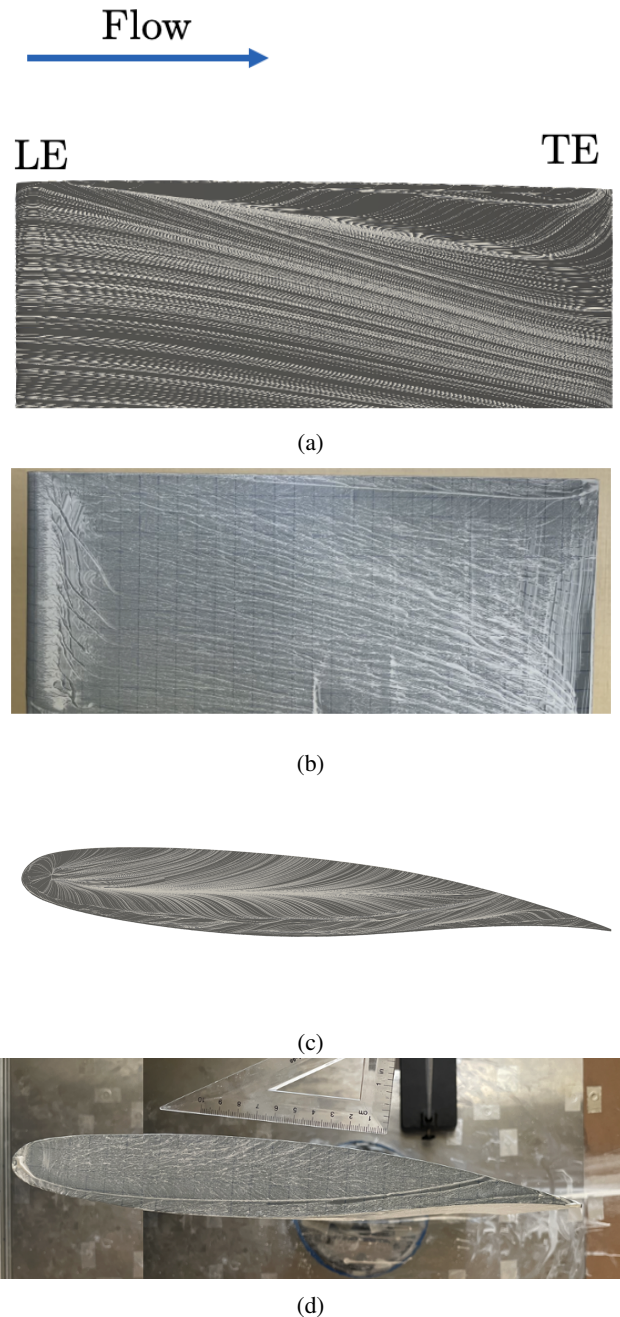


Figure. 7: Surface flow visualized on the supercritical airfoil model with $\alpha = 5°$, $Re = 6.2 \times 10^5$, $Ma = 0.09$. a) Simulated surface flow on the wing-tip suction surface. b) Experimental surface flow on the suction surface. c) Simulated surface flow at the side-edge. d) Experimental surface flow at the side-edge. Fig. a,b) are mirrored to align the flow direction.

the aerodynamic structures, specifically vortex shredding along the trailing edge and the side-edge vortex, the wave front propagating radially is still clearly visible and is centered around the core of the side-edge vortex. These wave fronts initially take a cylindrical shape but propagate away as duct modes after reflection from the walls.
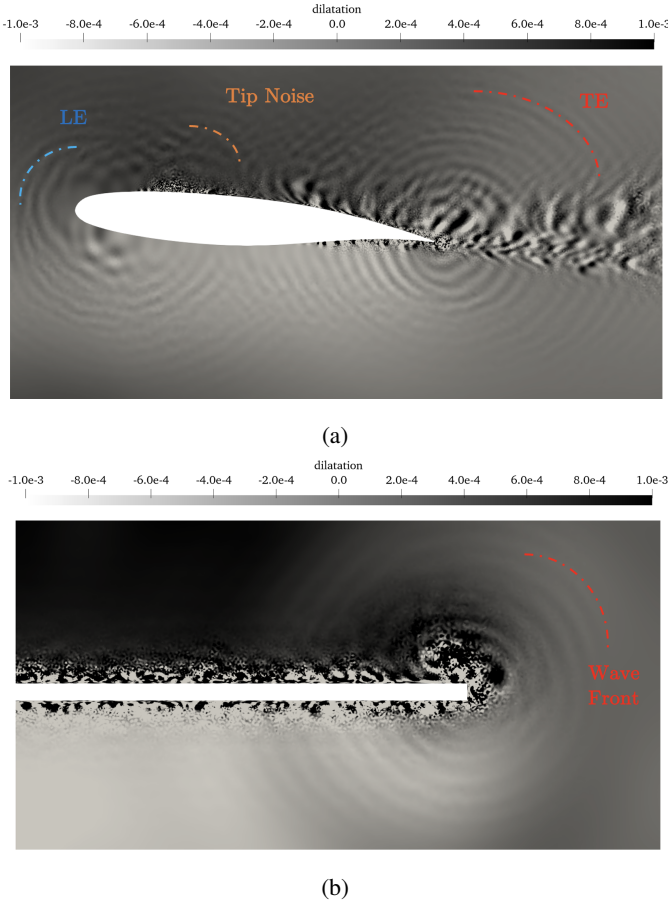


(a)



(b)

Figure. 8: Dilatation field - a) $0.06c$ from tip, b) $0.95c$ from trailing edge.

*B. Farfield Noise*

The acoustic propagation is modelled using the FW-H analogy based on wall-pressure fluctuations provided from the aerodynamic simulation [14]. The in-house code SherFWH developed at the Université de Sherbrooke was applied to compute the far-field acoustics based on the advance time formulation of Casalino and Najafi-Yazdi *et al.* [15]–[17]. The wall surface pressure is extracted at a sampling frequency of 100 kHz.

The simulated far-field narrowband spectra is compared with experimental results and shown in Fig. 9. The simulation and experimental spectra demonstrate similarities on the spectral trend. Specifically, the monotonic decrease in the spectra level with increasing frequency. The tonal humps in the simulation spectra corresponds to the propagation of the simulated wind tunnel modes whose cut-off frequencies are calculated by assuming the passage as a three-dimensional duct with cut-off frequencies $f_{c,(m,n)}$.
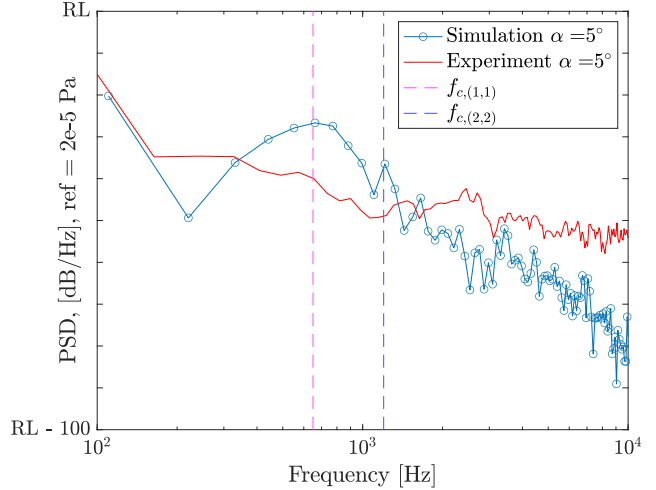


Figure. 9: Comparison of the far-field noise spectrum between simulation and experiment (distance between 2 tick marks on PSD represent 10 dB).

The agreement between the simulated and experimental spectra then deteriorates beyond the 4 kHz mark. One possible reason for this divergence is the use of the solid surface FW-H analogy, which assumes that the contribution of quadruple sources is negligible, including the self-noise of eddies induced by vortex shredding. This assumption is valid for low subsonic flows where the relative strength of eddy self-noise is small [18], [19], a condition that is satisfied with the freestream Mach number of 0.09 in this study. However, the complex vortex system depicted in Fig. 4b reveals continuous vortex interactions along the side-edge, and as quadruple noise is generated through vortex self-interactions, the contribution of quadruple turbulence-induced noise should be considered. Another reason for this divergence is the effect of Kevlar wall roughness noise, which is dominant at high frequencies in the experimental configuration. Effects of Kevlar transpiration and Kevlar self-noise were not captured since the simulation applied a hard-wall boundary condition to model the wind tunnel wall.

## V. Conclusion

An isolated supercritical airfoil was studied through a compressible wall-resolved Large Eddy Simulation to investigate the side-edge vortex structures, near-field wave patterns, and far-field acoustics. The analysis revealed the presence of primary, secondary, and tertiary vortices at the side edge, which merge into a coherent tip vortex. These vortices were shown to have a significant impact on the surface flow profile, with two distinct pressure peaks visible on the suction side $C_P$ plot and flow path lines revealing distinct profiles. Comparison of the simulation surface flow pathlines with oil flow visualization from the reference experiment demonstrated good agreement, particularly with respect to the flow separation line positions. The nearfield dilatation was observed to exhibit cylindrical waves originating from the leading edge, trailing edge, and vortex structures at the side edge. Finally, the FW-H acoustic

analogy was used to compute far-field noise, revealing the presence of dominant duct modes at mid frequencies. However, divergence in the acoustic spectra between the simulation and reference experiment was observed at high frequencies due to the neglect of quadruple turbulence-induced noise in the computation and the effect of Kevlar self-noise.

## REFERENCES

[1] W. Dobrzynski, "Almost 40 years of airframe noise research: what did we achieve?," *Journal of aircraft*, vol. 47, no. 2, pp. 353–367, 2010.

[2] M. Macaraeg, "Fundamental investigations of airframe noise," in *4th AIAA/CEAS Aeroacoustics Conference*, pp. AIAA–1998–2224, NASA Langley Research Center, 1998.

[3] M. R. Khorrami and B. A. Singer, "Stability analysis for noise-source modeling of a part-span flap," *AIAA Journal*, vol. 37, pp. 1206–1212, October 1999.

[4] K. Meadows, T. Brooks, W. Humphreys, W. Hunter, and C. Gerhold, "Aeroacoustic measurements of a wing-flap configuration," in *3rd AIAA/CEAS aeroacoustics conference*, pp. AIAA–1997–1595, 1997.

[5] T. F. Brooks and W. M. Humphreys, "Flap-edge aeroacoustic measurements and predictions," *Journal of Sound and Vibration*, vol. 261, pp. 31–74, September 2000.

[6] T. Imamura, S. Enomoto, and K. Yamamoto, "Noise simulation around NACA0012 wingtip using Large Eddy Simulation," *Transactions of the Japan Society for Aeronautical and Space Sciences*, vol. 55, no. 4, pp. 214–221, 2012.

[7] G. C. Deng, S. Baba, P. Lavoie, and S. Moreau, "Computational and experimental aeroacoustics of an isolated supercritical wingtip model," in *AIAA SCITECH 2023 Forum*, pp. AIAA–2023–1158, 2023.

[8] T. Schonfeld and M. Rudgyard, "Steady and unsteady flow simulations using the hybrid flow solver avbp," *AIAA journal*, vol. 37, no. 11, pp. 1378–1385, 1999.

[9] P. Roe, "Generalized formulation of tvd lax-wendroff schemes," tech. rep., 1984.

[10] D. H. Rudy and J. C. Strikwerda, "Boundary conditions for subsonic compressible navier-stokes calculations," *Computers & Fluids*, vol. 9, no. 3, pp. 327–338, 1981.

[11] E. Garnier, N. Adams, and P. Sagaut, *Large eddy simulation for compressible flows*. Springer Science & Business Media, 2009.

[12] ANSYS, "CFX 19.1," 2021.

[13] C. Mockett, T. Knacke, and F. Thiele, "Detection of initial transient and estimation of statistical error in time-resolved turbulent flow data," in *Proceedings of the 8th International Symposium on Engineering Turbulence Modelling and Measurements*, pp. 9–11, European Research Collaboration on Flow Turbulence and Combustion, 2010.

[14] J. F. Williams and D. L. Hawkings, "Sound generation by turbulence and surfaces in arbitrary motion," *Philosophical Transactions for the Royal Society of London. Series A, Mathematical and Physical Sciences*, pp. 321–342, 1969.

[15] D. Casalino, "An advanced time approach for acoustic analogy predictions," *Journal of Sound and Vibration*, vol. 261, no. 4, pp. 583–612, 2003.

[16] F. Farassat, "Derivation of formulations 1 and 1a of farassat," Tech. Rep. NASA TM-2007–214853, NASA Langley Research Center, 2007.

[17] A. Najafi-Yazdi, G. A. Brès, and L. Mongeau, "An acoustic analogy formulation for moving sources in uniformly moving media," *Proceedings of the Royal Society A: Mathematical, Physical and Engineering Sciences*, vol. 467, no. 2125, pp. 144–165, 2011.

[18] W. Devenport, R. Burdisso, A. Borgoltz, P. Ravetta, M. Barone, K. Brown, and M. Morton, "The kevlar-walled anechoic wind tunnel," *Journal of Sound and Vibration*, vol. 332, p. 3971–3991, 08 2013.

[19] S. Glegg and W. Devenport, *Aeroacoustics of low Mach number flows: fundamentals, analysis, and measurement*. Academic Press, 2017.